Ultrafast terahertz field control of electronic and structural interactions in vanadium dioxide

A. X. Gray *et al.*

Phys. Rev. B **98**, 045104 — Published 2 July 2018

DOI: 10.1103/PhysRevB.98.045104

Ultrafast THz Field Control of Electronic and Structural Interactions in Vanadium Dioxide

A. X. Gray[1,2,]*, M. C. Hoffmann[3], J. Jeong[4], N. P. Aetukuri[4], D. Zhu[3], H. Y. Hwang[5], N. C. Brandt[5], H. Wen[6], A. J. Sternbach[7,8], S. Bonetti[1], A. H. Reid[1], R. Kukreja[1,9], C. Graves[1,10], T. Wang[1,9], P. Granitzka[1,11], Z. Chen[1,12], D. J. Higley[1,10], T. Chase[1,10], E. Jal[1], E. Abreu[7,13], M. K. Liu[7,14], T.-C. Weng[15], D. Sokaras[15], D. Nordlund[15], M. Chollet[3], R. Alonso-Mori[3], H. Lemke[3], J. M. Glownia[3], M. Trigo[1], Y. Zhu[6], H. Ohldag[15], J. W. Freeland[6], M. G. Samant[4], J. Berakdar[16], R. D. Averitt[7,8], K. A. Nelson[5], S. S. P. Parkin[4], H. A. Dürr[1,17]*

[1]Stanford Institute for Materials and Energy Sciences, SLAC National Accelerator Laboratory, Menlo Park, California 94025, USA

[2]Department of Physics, Temple University, Philadelphia, Pennsylvania 19122, USA

[3]Linac Coherent Light Source, SLAC National Accelerator Laboratory, Menlo Park, California 94025, USA

[4]IBM Almaden Research Center, San Jose, CA 95120, USA

[5]Department of Chemistry, Massachusetts Institute of Technology, Cambridge, Massachusetts 02139, USA

[6]Advanced Photon Source, Argonne National Laboratory, Argonne, Illinois 60439, USA

[7]Department of Physics, Boston University, Boston, Massachusetts 02215, USA

[8]Department of Physics, The University of California at San Diego, La Jolla, California 92093, USA

[9]Department of Materials Science and Engineering, Stanford University, Stanford, California 94305, USA

[10]Department of Applied Physics, Stanford University, Stanford, California 94305

[11]Van der Waals-Zeeman Institute, University of Amsterdam, 1018XE Amsterdam, The Netherlands

[12]Department of Physics, Stanford University, Stanford, California 94305

[13]Institute for Quantum Electronics, ETH Zürich, 8006 Zürich, Switzerland

[14]Department of Physics and Astronomy, Stony Brook University, Stony Brook, NY 11794, USA

[15]Stanford Synchrotron Radiation Lightsource, SLAC National Accelerator Laboratory, Menlo Park, California 94025, USA

[16]Institut fur Physik, Martin-Luther-Universität Halle-Wittenberg, 06099 Halle/Saale, Germany

[17]Department of Physics and Astronomy, Uppsala University, P. O. Box 516, S-75120 Uppsala, Sweden

*E-mail: axgray@temple.edu, hermann.durr@physics.uu.se

ABSTRACT

Vanadium dioxide (VO_2), an archetypal correlated-electron material, undergoes an insulator-metal transition near room temperature that exhibits electron-correlation-driven and structurally-driven physics. Using ultrafast temperature- and fluence-dependent optical spectroscopy and x-ray scattering we show that multiple interrelated electronic and structural processes in the non-equilibrium dynamics in VO_2 can be disentangled in the time domain. Specifically, following intense sub-picosecond THz electric-field excitation, a partial collapse of the insulating gap occurs within the first picosecond. At temperatures sufficiently close to the transition temperature and for THz peak-fields above a threshold of approximately 1 MV/cm, this electronic reconfiguration initiates a change in lattice symmetry taking place on a slower timescale. We identify the kinetic energy increase of electrons tunneling in the strong electric field as the driving force, illustrating a novel method to control electronic and structural interactions in correlated materials on an ultrafast timescale.

1. INTRODUCTION

Ultrafast control of fundamental electronic and structural interactions in strongly-correlated oxide materials is a promising avenue toward realizing the next generation of faster and more energy-efficient electronic devices [1-5]. VO_2 is viewed as a potential key building block for such devices due to its near-room-temperature insulator-metal transition (IMT), which can be triggered on a sub-picosecond time scale [6-8]. Such rapid switching, along with dramatic changes in the electrical and optical properties [9-11], gives rise to a multitude of novel possibilities for logic and memory devices, some of which could potentially be transformative to modern technology and computing [2,12,13].

While a full understanding of the IMT in VO_2 remains a challenge, it is clear that both electron-electron correlations and electron-lattice interactions are relevant [14,15]. What is less clear is the extent to which correlation and structure can be disentangled, though evidence is mounting that a monoclinic metallic phase can be obtained under appropriate conditions [16-20]. As such, a concerted effort aimed at understanding and achieving decoupling of the electronic and structural transitions in VO_2 has gained significant momentum [17,18,21]. To further investigate these intriguing possibilities, it is crucial to interrogate the dynamics of the electronic and lattice structure under well-controlled excitation conditions and on the same samples.

Along these lines, recent developments in the field of ultrashort high-field THz pulse generation opened the door for triggering the IMT in VO_2 by nonresonant THz excitation of the electronic system at photon energies far below any of the relevant optical phonon modes or interband transitions [20]. A THz-pump THz-probe time-resolved study showed that the IMT in VO_2 can, in fact, be initiated with a THz electric field [22]. This experiment revealed that the transition is a multi-step process. However, the sub-picosecond electronic dynamics could not be temporally resolved nor were the structural dynamics measured.

We use THz excitation to initiate the IMT, which is probed using near-IR spectroscopy in combination with ultrafast hard x-ray scattering at the Linac Coherent Light Source (LCLS) [23,24]. We demonstrate that the various processes comprising the electric-field-induced electronic and structural phase transitions in VO_2 can occur on different time scales. Electronic structure switching in a $VO_2(001)$ film is observed to be virtually simultaneous with the sub-picosecond metamaterial-enhanced THz pulse and is induced by electric-field-assisted tunneling of valence electrons into the conduction band. For sufficiently high electric fields, $E \geq E_{\text{threshold}}$ (~1 MV/cm), this triggers the onset of the full transition to the rutile metallic state.

2. EXPERIMENT

2.1 THIN FILM AND METAMATERIALS SYNTHESIS

For our experiment, a high-quality crystalline 200 nm $VO_2(001)$ thin film was grown epitaxially on an $Al_2O_3(10\bar{1}0)$ substrate by pulsed laser deposition [25]. The temperature-dependent IMT was verified by electrical transport measurements in a Quantum Design DynaCool cryostat using a 4-terminal sensing method with aluminum wire contacts that were ultrasonically bonded directly to the surface of the VO_2 films (see Fig. 1(a)). Epitaxy and the monoclinic-rutile structural transition were verified with high-angular-resolution (<0.01°) x-ray diffraction (XRD) measurements using a Bruker D8 Discover system (see Fig. 1(b)) and high-resolution temperature-dependent XRD measurements carried out at the 7ID-C beamline of the Advanced Photon Source (see Fig. 1(a)). For the latter, the sample was mounted on a temperature-controlled stage with a control range from 250 to 450 K. The lattice Bragg peaks were characterized by θ-2θ scans in a six-circle diffractometer with a monochromatic 6.5 keV x-ray beam and an area detector (PILATUS 100K). Figures 1(a) and (b) show the results of these measurements confirming the bulk-like nature of our VO_2 films with the expected IMT and monoclinic-rutile (M1-R) structural transformation at 337 K, as defined by the heating curve. Static temperature-dependent near-IR (800 nm) transmission measurements confirm the optical response of the film, characterized by the decrease in transmission intensity across the IMT [15] (see Fig. 1 (c)).

Metamaterial antennae consisting of an array of 8.5 μm-wide Au lines (see Figs. 1(d) and 2(a)-(c)) were deposited on the sample via optical lithography in order to enhance the THz *E*-field at the sample, as described below. Transport measurements after the deposition (see Fig. 1(d)) show more than four orders of magnitude change in resistance across the IMT, thus indicating no degradation of film quality due to the fabrication process. Temperature-dependent XRD measurements carried out at LCLS prior to the time-resolved measurements confirm the structural transition of the patterned film (see Fig. 1(e)).

The optimal metamaterial geometry and dimensions were designed using the CST Microwave Studio full wave electromagnetic solver (see Fig. 2). The simulations used the time domain solver, performing a geometric parameter sweep to achieve the maximum terahertz field enhancement (see Fig. 2(d)) while maintaining compatibility with the experimental constraints. The antenna geometry was specifically optimized for the LCLS experiment, in order to provide a 4× enhancement across the spectrum of the incident THz pulse *E*-field (nominally up to 0.4 MV/cm) inside the 1.5 μm antenna gap (see Fig. 2(e)). Thus, maximum *E*-field peak strengths of up to 1.6 MV/cm (sufficient to initiate the IMT [22]) were achieved inside the gap at normal incidence. It is important to note that this maximum value is approximately 2.2 times lower than the damage threshold field (~3.5 MV/cm) reported in the prior study conducted for a similar film thickness, substrate material and the THz generation scheme [22]. Thus, no permanent damage to the film was expected to occur during the THz excitation.

Standard optical lithography techniques were used to fabricate the abovementioned metamaterials on a VO_2 film. Spin coating of 1.33 μm-thick photoresist (SPR670) and subsequent UV exposure and development was used to define the metamaterials. The part of the VO_2 film which was not covered by photoresist was milled away using an Ar ion beam with 100 eV energy. Metamaterial antenna electrodes composed of 2 nm Cr / 200 nm Au / 2 nm Cr were deposited on the etched area by ion beam deposition. After lift-off, the patterned sample was rinsed using isopropyl alcohol. Scanning electron microscopy (SEM) images of the resultant optimized periodic metamaterial pattern and its cross-sectional schematics are shown in Figs. 2(a)-(c).

2.2 TIME-RESOLVED MEASUREMENTS

Ultrafast THz-pump - near-IR and hard x-ray probe measurements were carried out non-concomitantly in the experimental geometries shown in Fig. 3(a). Both experiments used single-cycle THz pump pulses with peak *E*-field up to 0.4 MV/cm and central frequency of 0.6 THz, generated by the 20 mJ output of a 1 kHz, 100 fs Ti:Sapphire amplifier via optical rectification in a $LiNbO_3$ crystal using the tilted pulse-front technique [26-28].

THz-pump - near-IR-probe measurements of the electronic structure evolution were carried out in the collinear normal-incidence geometry as shown in Fig. 3(a). Part of the 800 nm beam generated by the Ti:Sapphire amplifier was utilized as a probe of the sample transmission with a standard ultrafast InGaAs diode used as a detector. The wavelength of 800 nm is sensitive to the interband transitions from the occupied $d_{\parallel}$ (a_{1g}) orbitals across the insulating gap and into the unoccupied π^* (e_g^{π}) states (see Fig. 3(b)). During the IMT, bonding and antibonding $d_{\parallel}$ states merge into a single band, while the π^* band shifts to lower energies. The two bands overlap in energy, and the resulting non-zero density of states at the Fermi level accounts for the metallic behavior and change in the transmission signal at 800 nm [15]. The THz-pump - near-IR-probe response of the substrate is negligible compared to that of the VO_2 film, as demonstrated by measurements on a bare $Al_2O_3(10\bar{1}0)$ sample within the same experimental setup (see Fig. 4).

THz-pump – x-ray probe structural dynamics experiments were carried out at the x-ray pump-probe (XPP) instrument of the LCLS. In order to measure the time-resolved lattice response of VO_2, the THz pump was incident on the sample collinearly with the 7 keV FEL x-ray beam at an incidence angle of ~38°, which is the Bragg angle for the rutile (002) diffraction peak, sensitive to the changes in atomic-layer spacing along the c_R axis (see Fig. 3(a)). In the static case, a temperature-induced transition results in a decay of the monoclinic $(40\bar{2})$ peak (M1) and growth of the rutile (002) peak (R), which is offset in q-space by 0.02 Å^{-1} due to the change in the average lattice spacing (see Fig. 3(c), as well as Fig. 1(e)). A large two-dimensional position-sensitive detector (CSPAD) [29] enables θ-2θ spectroscopic measurements of the rutile and monoclinic diffraction peaks by rotating the sample (θ) and measuring the intensities of the specular Bragg reflection spots (R and M1) while tracking their movement across the detector (2θ). The structural transition accompanied by dimerization of the neighboring V atoms along the out-of-plane c_R direction and tilting of the resultant V-V dimers along the rutile $[110]$ and $[1\bar{1}0]$ directions is depicted schematically in Fig. 3(d).

3. RESULTS

3.1 ELECTRONIC STRUCTURE EVOLUTION

Figure 5 shows the electronic response to THz excitation as measured by optical transmission. The onset of the electronic response is observed simultaneously with the THz excitation pulse shown in Fig. 5(a) exhibiting a rich multi-step evolution. In order to decouple the distinct electronic processes taking place within the first several picoseconds following THz excitation, we carried out a series of temperature- and fluence-dependent THz-pump - near-IR-probe measurements. Figures 5(a) and 5(b) depict time-delay traces of normalized near-IR transmission (at λ=800 nm) recorded for two different temperatures and for several THz pump excitation strengths expressed in terms of the peak E-field. The THz pulse waveform (not enhanced by metamaterials) was measured and calibrated via standard electro-optic sampling

[30], as shown in the outset plot above Fig. 5(a) displaying the profile observed in prior studies [22,31,32]. The maximum achieved enhanced peak *E*-field of 1.6 MV/cm was normalized to 100%, and the attenuated peak *E*-fields of 80% (1.28 MV/cm), 60% (0.96 MV/cm), *etc.* with respect to this nominal value were obtained using a pair of rotatable THz wire-grid polarizers.

Figure 5(a) shows *E*-field-dependent pump-probe time-delay traces recorded at room temperature (T_1=300 K), which is 37 K below the measured T_{IMT} of 337 K. As the data show, at temperatures far below the onset of the IMT, the dynamics is dominated by processes confined to the temporal window when the THz pulse is present in the sample (~1 ps). There is a substantial increase in the optical transmission of the film that follows in shape the square of the THz pulse waveform. This suggests an *E*-field-driven modification of the electronic structure leading to a transient decrease of the near-IR absorption analogous to what has been observed in dielectrics by Schultze *et al.* [3]. Essentially, a Wannier-Stark-like renormalization of the band structure results in a decrease in the joint density of states between occupied and unoccupied levels leading to the observed transmission increase [33-38]. The Wannier-Stark-like renormalization is independent of sample temperature and displays a nonlinear dependence on the strength of the *E*-field (Fig. 5(c)), consistent with prior experimental observations as well as with the theoretical picture [3,38]. It is important to note that additional time-resolved experiments utilizing direct probes of the valence and conduction bands with sub-THz-pulse-length resolution are required to unambiguously confirm the proposed picture of the Wannier-Stark effect assisting the IMT.

At strong enough fields, Wannier-Stark-like renormalization results in the mixing of the valence- and conduction-band electronic states leading to Zener-Keldysh-like interband tunneling of valence electrons at the valence-conduction-band anticrossings [38-42]. We observe the experimental fingerprint of such a non-thermal electronic tunneling process, characterized by an abrupt decrease in transmission due to prompt metallization coinciding with the transient peak attributed to the band renormalization. We emphasize that this effect is simultaneous with the exciting THz pulse and ceases once the THz pulse is no longer present in the sample (past *t*=1 ps). Importantly, this step-like tunneling feature is (*unlike* the *E*-field dependent band renormalization) highly temperature-dependent as evidenced by the differences between the data at T_1=300 K (Fig. 5(a)) and T_2=324 K (Fig. 5(b)). We speculate that the apparent increase in the efficiency of the interband tunneling processes near the T_{IMT} (Fig. 5(b)) could be attributed to changes in the electronic structure and, in particular, to the softening of strong electronic correlations at the onset of the IMT observed recently via temperature-dependent polarized x-ray absorption spectroscopy [43,44]. An unambiguous determination of the origin of this phenomenon requires an in-depth time-resolved temperature-dependent study.

At room temperature (T_1=300 K), the interband tunneling at high THz peak-fields induces a stable long-lived state with partially collapsed bandgap that persists for picoseconds after the THz pulse (Fig. 5(a)). This observation is consistent with the recent work by Mayer *et al.* [45] wherein the IMT in VO_2 was induced by multi-THz transients. As we tune the temperature closer to T_{IMT} (up to T_2=324 K), tunneling becomes more efficient (see respective delay traces in Fig. 5(b)) without, however, altering the temporal behavior. Finally, above a peak THz field of 1.0 MV/cm (±0.1 MV/cm) a *third* process sets in, characterized by an exponential decrease with time in near-IR transmission after *t*=1 ps. Above this threshold field value, this exponential process begins to dominate the IMT dynamics, driving the film towards the metallic phase over a multi-picosecond time scale. Observation of this slower dynamics is consistent with the measurements by Liu *et al.* [22] (also obtained at the temperature of 324 K) where the energy density deposited by a THz pulse was sufficient to drive electron-phonon thermalization and heating towards (and above) T_{IMT}. We consider this picture in more detail in the following paragraphs.

Since the Wannier-Stark-like renormalization does not show a significant temperature-dependence, as evidenced by the overlaid plots of the *E*-field-dependent peak intensities for 300 K and 324 K in Fig. 5(c), we can subtract this contribution from the higher-temperature data using corresponding room-temperature spectra. This data analysis enables the extraction of the temporal shape and amplitude of the tunneling breakdown dynamics in VO_2 during the first picosecond of the IMT. As shown in Fig. 5(d), the abrupt decrease in transmission follows a simple step function broadened by the THz pulse duration, consistent with ultrafast non-thermal field-induced tunneling as described above [45]. For high THz fluences this process is followed by slower metallization dynamics characterized by an exponential decay where the band-gap collapses with a time constant of approximately 6 ps (Fig. 5(d)).

Figure 5(e) shows the amplitude versus field-strength of the step-like and exponential features from Fig. 5(d). The points were obtained by simultaneous fitting of the delay traces with the combination of a simple step function broadened by the THz pulse duration (fixed value of 1 ps) and an exponential decay function. Best-fit values of the step and exponent amplitudes, as well as the corresponding error bars, are shown in Fig. 5(e) for all measured delay traces. Typical example of the fit (for E = 1.6 MV/cm) is shown as the dashed curves overlaying the experimental data (purple symbols) in Fig. 5(d).

A clear difference in the functional dependence of these two features suggests different electronic origins. The step-function amplitude (red markers in Fig. 5(e)) exhibits exponential behavior (versus *E*-field) consistent with nonresonant Zener tunneling [39,41]. It is measurable even at moderate peak-fields (0.32 MV/cm). Best fit to an exponential function is shown with a red solid line. In contrast, a clear threshold behavior is observed for the exponential amplitude (blue curve). The threshold field sufficient to drive the electronic system through the point of no return is estimated to be approximately 1 MV/cm (blue/purple marker). Above this critical field, the IMT progresses exponentially with a steep field-dependence (purple markers) resulting in metallization of a significant fraction of the film.

While Fig. 5 focuses on the time delays relevant to the key processes involved in the *initiation* of the IMT in VO_2 (0 - 8 ps), in Fig. 6 we show a typical THz-pump - near-IR-probe trace collected for longer time delays (up to 500 ps), which include further growth and subsequent relaxation of the metallic phase. This delay trace, showing the long-term electronic response to THz excitation, can be directly compared to the structural dynamics evolution plots shown in the next section. We note that during the growth phase (1 - 175 ps) the 800-nm transmission decays monotonically, with the exception of a sharp feature observed at *ca.* +9.5 ps. This feature is an “echo” artefact, arising due to the reflection of the THz pulse from the backside of the substrate in the normal-incidence geometry.

3.2 STRUCTURAL DYNAMICS

Figure 7 shows the temporal evolution of the monoclinic-rutile structural transformation during the first 500 ps following THz pump excitation for two sample base temperatures. Data points were obtained by integrating the intensities of the monoclinic (M1) and rutile (R) scattering peaks measured via θ-2θ scans (shown in units of q_c in the insets) at a given time delay. In order to account for any instrumental drift during the scan, every forty-first shot was recorded without the excitation laser pulse (I_{OFF}) and used as a continuous equilibrium ‘laser-off’ reference. Detector data for each x-ray pulse was corrected (via simple subtraction) by the reference dark-current detector image and then normalized using the shot-to-shot x-ray pulse intensity monitor [46]. In order to account for any additional intensity fluctuations between individual pulses, a flat diffuse detector background sampled from a region on the image close to but separated from the M1 and R peaks was subtracted for each shot. A weighted average of all the shots for each value of q_c was then calculated based on the x-ray pulse intensity monitor. The resultant experimental θ-2θ spectra (circular markers in the insets) were then fitted using simple gaussians (solid lines), and the extracted intensities were plotted as functions of time delay (main panels (a)-(d)).

The measurements shown in panels (a) and (b) were carried out at the sample temperature of 324 K (T_{IMT}-13 K), at which approximately 2.7% of the VO_2 film under the x-ray measurement spot has already undergone the transition. Thus, prior to the THz electric-field pulse arrival at t = 0 ps, approximately 97.3% of the sample under the x-ray probe spot was still in the low-temperature monoclinic phase, and approximately 2.7% of the sample was already in the high-temperature rutile phase. The measurements shown in panels 7(c)-(d) were carried out at a higher base temperature of 332 K (T_{IMT}-5 K), at which approximately 27% of the VO_2 film is already transformed from the monoclinic to the rutile phase. While the overall shape of the monoclinic and rutile data is qualitatively similar for the two base temperatures (see section 4 for further discussion), there is a clear deviation for early times for the rutile data (see top inset of Fig. 7(d)). The initial dip in the rutile diffraction intensity at 332 K demonstrates increased thermal lattice heating following the THz pump, likely due to THz driven currents in the metallic regions (see discussion below).

4. DISCUSSION

The results of our THz-pump - near-IR-probe experiments suggest the following scenario (Fig. 5(f)). Below $E_{threshold}$, the applied field induces Wannier-Stark band renormalization accompanied by Zener-Keldysh-like interband tunneling. At times longer than the pulse duration, the flat plateau that is observed in Fig. 5(a) arises from carriers that have tunneled into the conduction band and do not recombine for many picoseconds. In the language of correlated electron materials, the tunneling creates double occupancy sites with a finite density of states at E_F – that is, there is a partial collapse of the Mott-Hubbard gap. In this E-field range below $E_{threshold}$ and on the timescales accessed in Fig. 5 there is no observable increase or decrease in the signal beyond 1 ps. As we raise the sample temperature closer to the onset of the IMT (to $T_2=T_{IMT}$-13K) electronic correlations are softened [43] – a phenomenon which is unique to strongly-correlated oxides, such as VO_2, and not observed for a typical band insulator [3]. This leads to more efficient tunneling accompanied by a concurrent band-gap collapse when double occupancies are formed, and to a commensurate increase in the carrier density. Subsequently, the THz electric field accelerates these carriers, which then relax though electron-phonon collisions. For sufficiently high fields, above $E_{threshold}$, this increases the lattice temperature initiating the IMT towards the rutile metallic phase. This corresponds to the exponentially decreasing term in Fig. 5(d) (magenta line).

In the grazing-incidence Bragg geometry necessary for the THz-pump - x-ray probe measurements (Fig. 3(a)), the enhanced E-field peak strength is determined to be 1.0 MV/cm (±0.1 MV/cm) using basic geometric considerations. At this field strength, the THz excitation drives VO_2 towards the threshold above which electron-lattice interactions trigger the change in lattice symmetry (Figs. 5(d)-(e)). Thus, the long-term (hundreds-of-picoseconds) structural dynamics shown in Figs. 7(a)-(b) is characterized, as expected, by the decay of the monoclinic phase (a) and a concomitant growth of the rutile phase (b). We note that during the first ~30 ps of the THz-driven transition the change in lattice symmetry manifests, initially, as an increase of the monoclinic peak intensity. Specifically, the monoclinic peak intensity grows for ~30 ps before eventually decreasing and, further, is not accompanied by a decrease in the intensity of the rutile peak. This suggests that a new monoclinic phase of VO_2, characterized by a higher structure factor, may be forming at the onset of the structural transition. A possible two-step scenario, involving initial dilation of the V-V dimers at the onset of the transition, has been proposed in a prior ultrafast electron diffraction study of the optically-induced IMT in VO_2 [47]. However, the observed timescales for the optically-induced dynamics in Ref. [47] differ significantly from ours (THz-induced). Thus, further investigations involving concomitant measurements of additional diffraction peaks that are sensitive to the in-plane lattice constants of the film are required to unambiguously solve for the motion of the V-V dimers during the onset of the transition. Such measurements were not possible in the current experimental setup.

Finally, both electronic and structural phase separation scenarios in VO_2 have been previously observed both statically and dynamically during temperature-driven transition by scanning near-field optical and infrared microscopy [48-50] and scanning probe x-ray diffraction [51]. Thus, the presence of a small amount of rutile phase (approximately 2.7%) at the base temperature of 324 K (T_{IMT}-13 K) raises an important question as to whether selective heating due to THz-driven currents in the conducting regions and subsequent thermal diffusion could account for the observed slow (hundreds-of-picoseconds) structural dynamics. To address this question, we show in Figs. 7(c)-(d) time-resolved XRD data obtained at a higher base temperature of 332 K (T_{IMT}-5 K), at which approximately 27% of the VO_2 film is already transformed from the monoclinic to the rutile phase, and thus a much higher metallic volume fraction can be affected by the THz pump. As can be unambiguously seen in Fig. 7(d) and its top inset, during the first 15 ps the rutile XRD signal is attenuated due to preferential heating of the lattice in these regions (Debye-Waller effect). In contrast, for the lower base temperature in Figs. 7(a)-(b) no such effect is observed within the uncertainty of the measurement. This suggests that preferential excitation of the already present metallic rutile puddles requires a certain size of such regions, as it is satisfied at 332 K. However, this mechanism can be ruled out to be the dominant process for the much smaller rutile patches present at 324 K. Finally, heating of the Au metamaterial stripes can be neglected since heat transport, with typical propagation speeds on the order of 1 nm/ps [52], takes hundreds of ps to cover the whole VO_2 material in the 1.5 μm wide metamaterial gap. We also would like to point out that the different amount of rutile VO_2 generated by THz heating for the two base temperatures shown in Fig. 7 points to a more efficient absorption of THz energy into preexisting rutile compared to monoclinic VO_2 areas. Overall, the THz energy absorbed in our experiment is smaller than that for typical optical excitation energies [22].

Further investigations of the sub-picosecond lattice dynamics near time-zero are required to determine the three-dimensional lattice response during the intense THz pulse, which reaches its peak value at t=+0.2 ps (within a 2 ps-long window between the measured time delays of -1 ps and +1 ps). Additional high-resolution and high-statistics time-resolved x-ray diffraction measurements should be carried out to determine the lattice response during the initial stages of the IMT (1 - 8 ps). Furthermore, the possible existence of the intermediate M2 phase, shown to be present in strained films [10], must be considered in future studies of strained films. Finally, effects of the multiple THz reflections from the back surface of the substrate need to be considered at longer delay times.

5. SUMMARY AND CONCLUSIONS

In conclusion, our experiments show that various processes in the non-equilibrium electronic and structural dynamics in VO_2 can be disentangled in the time domain by inducing the IMT with an intense nonresonant THz pulse and probing with near-IR and hard x-ray pulses. The primary trigger for the electric-field-initiated transition is shown to be Zener-Keldysh-like tunneling assisted by Wannier-Stark-like band renormalization. At temperatures sufficiently close to T_{IMT} and for THz peak-fields above a threshold of approximately 1 MV/cm the THz electric field accelerates the carriers, which increases the lattice temperature initiating the transition towards the rutile metallic phase. This is a result of softening of electronic correlations and of efficient energy transfer to the lattice from carrier acceleration and electron-phonon collisions. The rich multi-dimensional landscape resulting from the interplay of the Mott and Peierls physics provides a pathway to achieving efficient THz switching in strongly-correlated oxides via ultrafast electric-field excitation.

Research at Stanford was supported through the Stanford Institute for Materials and Energy Sciences (SIMES) under contract DE-AC02-76SF00515. Use of the Linac Coherent Light Source (LCLS), SLAC National Accelerator Laboratory, is supported by the U.S. Department of Energy, Office of Science, Office of Basic Energy Sciences under Contract No. DE-AC02-76SF00515. Research by the MIT group was supported in part by Office of Naval Research Grant No. N00014-13-1-0509 and National Science Foundation Grant No. CHE-1111557. Work at Argonne was supported by the US Department of Energy, Office of Science, Office of Basic Energy Sciences, under Contract No. DE-AC02-06CH11357. R.D.A. acknowledges support from the U.S. Department of Energy, Office of Science, Office of Basic Energy Sciences under Grant No. DE-FG02-09ER46643. E.A. acknowledges support from Fundação para a Ciência e a Tecnologia, Portugal, through doctoral degree fellowship SFRH/ BD/ 47847/ 2008. J.B. is supported by the DFG under grant SFB762. S.B. acknowledges support from the Knut and Alice Wallenberg Foundation.

REFERENCES

1. C. H. Ahn, J.-M. Triscone, J. Mannhart, Electric field effect in correlated oxide systems. *Nature* **424**, 1015 (2003).
2. Z. Yang, C. Ko, S. Ramanathan, Oxide Electronics Utilizing Ultrafast Metal-Insulator Transitions. *Annu. Rev. Mater. Res.* **41**, 336 (2011).
3. M. Schultze, E. M. Bothschafter, A. Sommer, S. Holzner, W. Schweinberger, M. Fiess, M. Hofstetter, R. Kienberger, V. Apalkov, V. S. Yakovlev, M. I. Stockman, F. Krausz, Controlling dielectrics with the electric field of light. *Nature* **493**, 75 (2013).
4. S. de Jong, R. Kukreja, C. Trabant, N. Pontius, C. F. Chang, T. Kachel, M. Beye, F. Sorgenfrei, C. H. Back, B. Bräuer, W. F. Schlotter, J. J. Turner, O. Krupin, M. Doehler, D. Zhu, M. A. Hossain, A. O. Scherz, D. Fausti, F. Novelli, M. Esposito, W. S. Lee, Y. D. Chuang, D. H. Lu, R. G. Moore, M. Yi, M. Trigo, P. Kirchmann, L. Pathey, M. S. Golden, M. Buchholz, P. Metcalf, F. Parmigiani, W. Wurth, A. Föhlisch, C. Schüßler-Langeheine, H. A. Dürr, Speed limit of the insulator–metal transition in magnetite. *Nature Materials* **12**, 882 (2013).
5. T. Kampfrath, K. Tanaka, K. A. Nelson, Resonant and nonresonant control over matter and light by intense terahertz transients. *Nature Photonics* **7**, 680 (2013).
6. F. J. Morin, Oxides which show a metal-to-insulator transition at the Neel temperature. *Phys. Rev. Lett.* **3**, 34 (1959).
7. A. Cavalleri, Cs. Tóth, C. W. Siders, J. A. Squier, F. Ráksi, P. Forget, J. C. Kieffer, Femtosecond Structural Dynamics in VO_2 during an Ultrafast Solid-Solid Phase Transition. *Phys. Rev. Lett.* **87**, 237401 (2001).
8. C. Kübler, H. Ehrke, R. Huber, R. Lopez, A. Halabica, R. F. Haglund, Jr., A. Leitenstorfer, Coherent Structural Dynamics and Electronic Correlations during an Ultrafast Insulator-to-Metal Phase Transition in VO_2. *Phys. Rev. Lett.* **99**, 116401 (2007).
9. M. M. Qazilbash, A. A. Schafgans, K. S. Burch, S. J. Yun, B. G. Chae, B. J. Kim, H. T. Kim, D. N. Basov, Electrodynamics of the vanadium oxides VO_2 and V_2O_3. *Phys. Rev. B* **77**, 115121 (2008).

10. J. H. Park, J. M. Coy, T. S. Kasirga, C. Huang, Z. Fei, S. Hunter, D. H. Cobden, Measurement of a solid-state triple point at the metal–insulator transition in VO_2. *Nature* **500**, 431–434 (2013).

11. N. B. Aetukuri, A. X. Gray, M. Drouard, M. Cossale, L. Gao, A. H. Reid, R. Kukreja, H. Ohldag, C. A. Jenkins, E. Arenholz, H. A. Dürr, M. Samant, S. S. P. Parkin, Control of the Metal-Insulator Transition in Vanadium Dioxide by Modifying Orbital Occupancy. *Nature Physics* **9**, 661 (2013).

12. S. Cueff, D. Li, Y. Zhou, F. J. Wong, J. A. Kurvits, S. Ramanathan, R. Zia, Dynamic control of light emission faster than the lifetime limit using VO_2 phase-change. *Nature Comm.* **6**, 8636 (2015).

13. N. Shukla, A. V. Thathachary, A. Agrawal, H. Paik, A. Aziz, D. G. Schlom, S. K. Gupta, R. Engel-Herbert, S. Datta, A steep-slope transistor based on abrupt electronic phase transition. *Nature Comm.* **6**, 7812 (2015).

14. J. B. Goodenough, The two components of crystallographic transition in VO_2. *J. Solid State Chem.* **3**, 490–500 (1971).

15. A. Cavalleri, Th. Dekorsy, H. H. W. Chong, J. C. Kieffer, R. W. Schoenlein, Evidence for a structurally-driven insulator-to-metal transition in VO_2: A view from the ultrafast timescale. *Phys. Rev. B* **70**, 161102(R) (2004).

16. S. Zhang, J. Y. Chou, L. J. Lauhon, Direct Correlation of Structural Domain Formation with the Metal Insulator Transition in a VO_2 Nanobeam. *Nano Lett.* **9**, 4527-4532 (2009).

17. Z. Tao, T.-R. T. Han, S. D. Mahanti, P. M. Duxbury, F. Yuan, C.-Y. Ruan, K. Wang, Junqiao Wu, Decoupling of Structural and Electronic Phase Transitions in VO_2. *Phys. Rev. Lett.* **109**, 166406 (2012).

18. J. Laverock, S. Kittiwatanakul, A.□A. Zakharov, Y.□R. Niu, B. Chen, S.□A. Wolf, J.□W. Lu, K.□E. Smith, Direct Observation of Decoupled Structural and Electronic Transitions and an Ambient Pressure Monocliniclike Metallic Phase of VO_2. *Phys. Rev. Lett.* **113**, 216402 (2014).

19. V. R. Morrison, R. P. Chatelain, K. L. Tiwari, A. Hendaoui, A. Bruhács, M. Chaker, B. J. Siwick, A photoinduced metal-like phase of monoclinic VO_2 revealed by ultrafast electron diffraction. *Science* **346**, 445-448 (2014).

20. S.-H. Kim, B.-J. Kim, T.-Y. Jeong, Y.-S. Lee, K.-J. Yee, Coherent phonon spectroscopy of the phase transition in VO_2 single crystals and thin films. *J. Appl. Phys.* **117**, 163107 (2015).

21. L. Whittaker, C. J. Patridge, S. Banerjee, Microscopic and Nanoscale Perspective of the Metal−Insulator Phase Transitions of VO_2: Some New Twists to an Old Tale. *J. Phys. Chem. Lett.* **2**, 745–758 (2011).

22. M. Liu, H. Y. Hwang, H. Tao, A. C. Strikwerda, K. Fan, G. R. Keiser, A. J. Sternbach, K. G. West, S. Kittiwatanakul, J. Lu, S. A. Wolf, F. G. Omenetto, X. Zhang, K. A. Nelson, R. D. Averitt, Terahertz-field-induced insulator-to-metal transition in vanadium dioxide metamaterial. *Nature* **487**, 345 (2012).

23. M. C. Hoffmann, J. J. Turner, Ultrafast X-ray Experiments Using Terahertz Excitation. *Synchrotron Rad. News* **25**, 17-24 (2012).

24. M. Chollet, R. Alonso-Mori, M. Cammarata, D. Damiani, J. Defever, J. T. Delor, Y. Feng, J. M. Glownia, J. B. Langton, S. Nelson, K. Ramsey, A. Robert, M. Sikorski, S. Song, D. Stefanescu, V. Srinivasan, D. Zhu, H. T. Lemke, D. M. Fritz, The X-ray Pump-Probe instrument at the Linac Coherent Light Source. *J. Synchrotron Rad.* **22**, 503 (2015).

25. J. Jeong, N. Aetukuri, T. Graf, T. D. Schladt, M. G. Samant, S. S. P. Parkin, Suppression of Metal-Insulator Transition in VO_2 by Electric Field–Induced Oxygen Vacancy Formation. *Science* **339**, 1402-1405 (2013).

26. J. Hebling, G. Almási, I. Z. Kozma, J. Kuhl, Velocity matching by pulse front tilting for large area THz-pulse generation. *Opt. Express* **10**, 1161 (2002).

27. A. G. Stepanov, J. Kuhl, I. Z. Kozma, E. Riedle, G. Almási, J. Hebling, Scaling up the energy of THz pulses created by optical rectification. *Opt. Express* **13**, 5762 (2005).

28. J. Hebling, K-L. Yeh, M. C. Hoffmann, B. Bartal, K. A. Nelson, Generation of high-power terahertz pulses by tilted-pulse-front excitation and their application possibilities. *J. Opt. Soc. Am. B* **25**, B6 (2008).

29. S. Herrmann, S. Boutet, B. Duda, D. Fritz, G. Haller, P. Hart, R. Herbst, C. Kenney, H. Lemke, M. Messerschmidt, J. Pines, A. Robert, M. Sikorski, G. Williams, CSPAD-140k: A versatile detector for LCLS experiments. *Nucl. Instrum. Meth. A* **718**, 550 (2013).

30. P. Planken, H. Nienhuys, H. Bakker, T. Wenckebach, Measurement and calculation of the orientation dependence of terahertz pulse detection in ZnTe. *J. Opt. Soc. Am. B* **18**, 313–317 (2001).

31. A. Dienst, M. C. Hoffmann, D. Fausti, J. C. Petersen, S. Pyon, T. Takayama, H. Takagi, A. Cavalleri, Bi-directional ultrafast electric-field gating of interlayer charge transport in a cuprate superconductor. *Nature Photonics* **5**, 485–488 (2011).

32. A. Dienst, E. Casandruc, D. Fausti, L. Zhang, M. Eckstein, M. Hoffmann, V. Khanna, N. Dean, M. Gensch, S. Winnerl, W. Seidel, S. Pyon, T. Takayama, H. Takagi, A. Cavalleri, Optical excitation of Josephson plasma solitons in a cuprate superconductor. *Nature Materials* **12**, 535–541 (2013).

33. G. H. Wannier, Elements of Solid State Theory. Elements 173–177 (Cambridge Univ. Press, 1959).

34. G. H. Wannier, Wave Functions and Effective Hamiltonian for Bloch Electrons in an Electric Field. *Phys. Rev.* **117**, 432 (1960).

35. J. Bleuse, G. Bastard, P. Voisin, Electric-field-induced localization and oscillatory electro-optical properties of semiconductor superlattices. *Phys. Rev. Lett.* **60**, 220–223 (1988).

36. E. E. Mendez, F. Agulló-Rueda, J. M. Hong, Stark Localization in GaAs-GaAlAs Superlattices under an Electric Field. *Phys. Rev. Lett.* **60**, 2426 (1988).

37. E. E. Mendez, G. Bastard, Wannier-Stark ladders and Bloch oscillations in superlattices. *Phys. Today* **46**, 34 (1993).

38. A. Schiffrin, T. Paasch-Colberg, N. Karpowicz, V. Apalkov, D. Gerster, S. Mühlbrandt, M. Korbman, J. Reichert, M. Schultze, S. Holzner, J. V. Barth, R. Kienberger, R. Ernstorfer, V. S. Yakovlev, M. I. Stockman, F. Krausz, Optical-field-induced current in dielectrics. *Nature* **493**, 70 (2013).

39. C. Zener, H. H. Wills, *Proc. R. Soc. London, Ser. A* **145**, 523 (1934).

40. L. V. Keldysh, Behavior of non-metallic crystals in strong electric fields. *Sov. J. Exp. Theor. Phys.* **6**, 763 (1958).

41. B. Rosam, K. Leo, M. Glück, F. Keck, H. J. Korsch, F. Zimmer, Lifetime of Wannier-Stark states in semiconductor superlattices under strong Zener tunneling to above-barrier bands. *Phys. Rev. B* **68**, 125301 (2003).

42. S. Ghimire, G. Ndabashimiye, A. D. DiChiara, E. Sistrunk, M. I. Stockman, P. Agostini, L. F. DiMauro, D. A. Reis, Strong-field and attosecond physics in solids. *J. Phys. B: At. Mol. Opt. Phys.* **47**, 204030 (2014).

43. A. X. Gray, J. Jeong, N. P. Aetukuri, P. Granitzka, Z. Chen, R. Kukreja, D. Higley, T. Chase, A. H. Reid, H. Ohldag, M. A. Marcus, A. Scholl, A. T. Young, A. Doran, C. A. Jenkins, P. Shafer, E. Arenholz, M. G. Samant, S. S. P. Parkin, H. A. Dürr, Correlation-Driven Insulator-Metal Transition in Near-Ideal Vanadium Dioxide Films. *Phys. Rev. Lett.* **116**, 116403 (2016).

44. L. H. Yeo, A. Srivastava, M. A. Majidi, R. Sutarto, F. He, S. M. Poh, C. Diao, X. Yu, M. Motapothula, S. Saha, S. Ojha, D. Kanjilal, P. E. Trevisanutto, M. B. H. Breese, T. Venkatesan, A. Rusydi, Anomalous spectral-weight transfers unraveling oxygen screening and electronic correlations in the insulator-metal transition of VO_2. *Phys. Rev. B* **91**, 081112(R) (2015).

45. B. Mayer, C. Schmidt, A. Grupp, J. Bühler, J. Oelmann, R. E. Marvel, R. F. Haglund, Jr., T. Oka, D. Brida, A. Leitenstorfer, A. Pashkin, Tunneling breakdown of a strongly correlated insulating state in VO_2 induced by intense multiterahertz excitation. *Phys. Rev. B* **91**, 235113 (2015).

46. Y. Feng, J. M. Feldkamp, D. M. Fritz, M. Cammarata, R. Aymeric, C. Caronna. H. T. Lemke, D. Zhu, S. Lee, S. Boutet, G. Williams, K. Tono, M. Yabashi, J. B. Hastings, A single-shot intensity-position monitor for hard X-ray FEL sources, *Proc. SPIE* **8140**, 81400Q (2011).

47. P. Baum, D.-S. Yang, A. H. Zewail, 4D Visualization of Transitional Structures in Phase Transformations by Electron Diffraction. *Science* **318**, 788-792 (2007).

48. M. M. Qazilbash, M. Brehm, B.-G. Chae, P.-C. Ho, G. O. Andreev, B.-J. Kim, S. J. Yun, A. V. Balatsky, M. B. Maple, F. Keilmann, H.-T. Kim, D. N. Basov, Mott Transition in VO_2 Revealed by Infrared Spectroscopy and Nano-Imaging. *Science* **318**, 1750 (2007).
49. M. K. Liu, M. Wagner, E. Abreu, S. Kittiwatanakul, A. McLeod, Z. Fei, M. Goldflam, S. Dai, M. M. Fogler, J. Lu, S. A. Wolf, R. D. Averitt, D. N. Basov, Anisotropic Electronic State via Spontaneous Phase Separation in Strained Vanadium Dioxide Films. *Phys. Rev. Lett.* **111**, 096602 (2013).
50. B. T. O'Callahan, A. C. Jones, J. H. Park, D. H. Cobden, J. M. Atkin, M. B. Raschke, Inhomogeneity of the ultrafast insulator-to-metal transition dynamics of VO_2. *Nature Comm.* **6** 6849 (2015).
51. M. M. Qazilbash, A. Tripathi, A. A. Schafgans, B.-J. Kim, H.-T. Kim, Z. Cai, M. V. Holt, J. M. Maser, F. Keilmann, O. G. Shpyrko, D. N. Basov, Nanoscale imaging of the electronic and structural transitions in vanadium dioxide. *Phys. Rev. B* **83**, 165108 (2011).
52. Y. Zhu, Z. Cai, P. Chen, Q. Zhang, M. J. Highland, I. W. Jung, D. A. Walko, E. M. Dufresne, J. Jeong, M. G. Samant, S. S. P. Parkin, J. W. Freeland, P. G. Evans, H. Wen, Mesoscopic structural phase progression in photo-excited VO_2 revealed by time-resolved x-ray diffraction microscopy. *Sci. Rep.* **6**, 21999 (2016).

FIG. 1

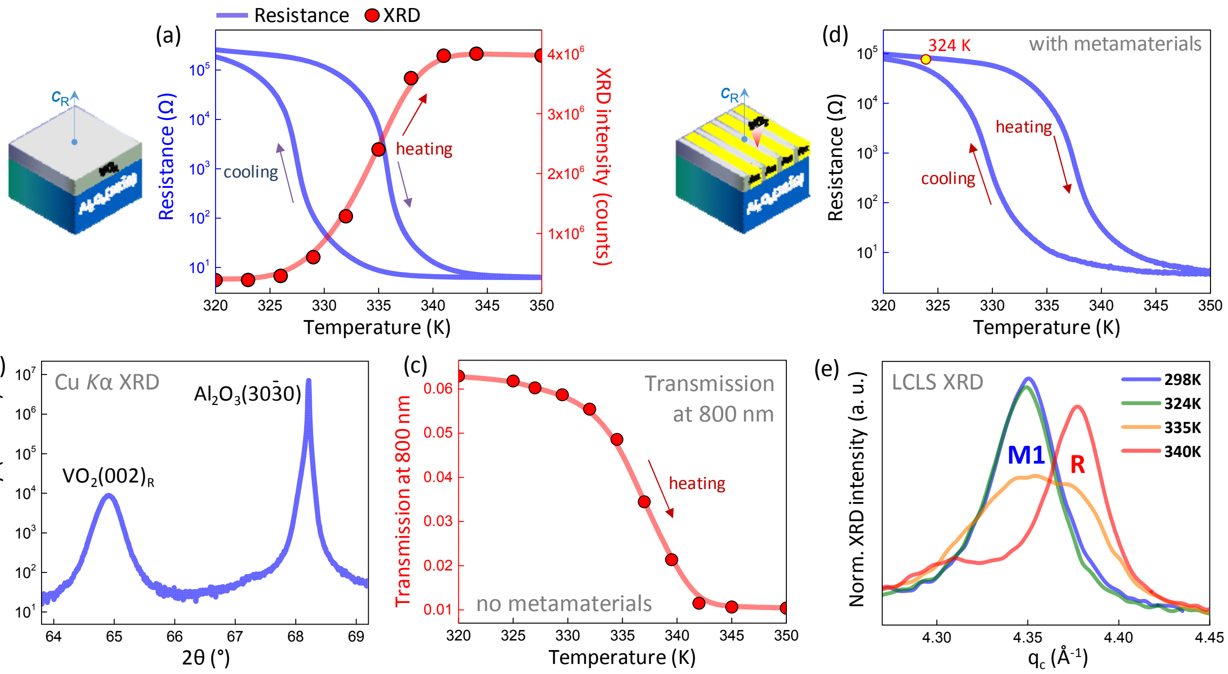

FIG. 1. Static resistance and x-ray diffraction characterization of the 200 nm $VO_2(001)$ film deposited on $Al_2O_3(10\bar{1}0)$ substrate. (a) Resistance versus temperature curves (blue) showing the insulator-metal transition during both heating and cooling cycles for the unpatterned film. Also shown is the intensity of the $VO_2(002)_R$ diffraction peak measured with synchrotron radiation and plotted as a function of temperature. (b) High-resolution Cu *K*α θ-2θ x-ray diffraction pattern showing both the substrate and the film Bragg peaks. (c) Static near-IR (800 nm) transmission versus temperature measured on the unpatterned film during the heating cycle. Temperature scale was adjusted to account for the difference in the temperature calibration between the different sample holders. (d) Resistance versus temperature curves measured after patterning the VO_2 film with Au metamaterials. Starting (base) temperature for the pump-probe measurements (324 K) is marked with a yellow circle. (e) Temperature-dependent x-ray diffraction scans of the VO_2 film peak carried out at LCLS prior to time-resolved measurements.

FIG. 2

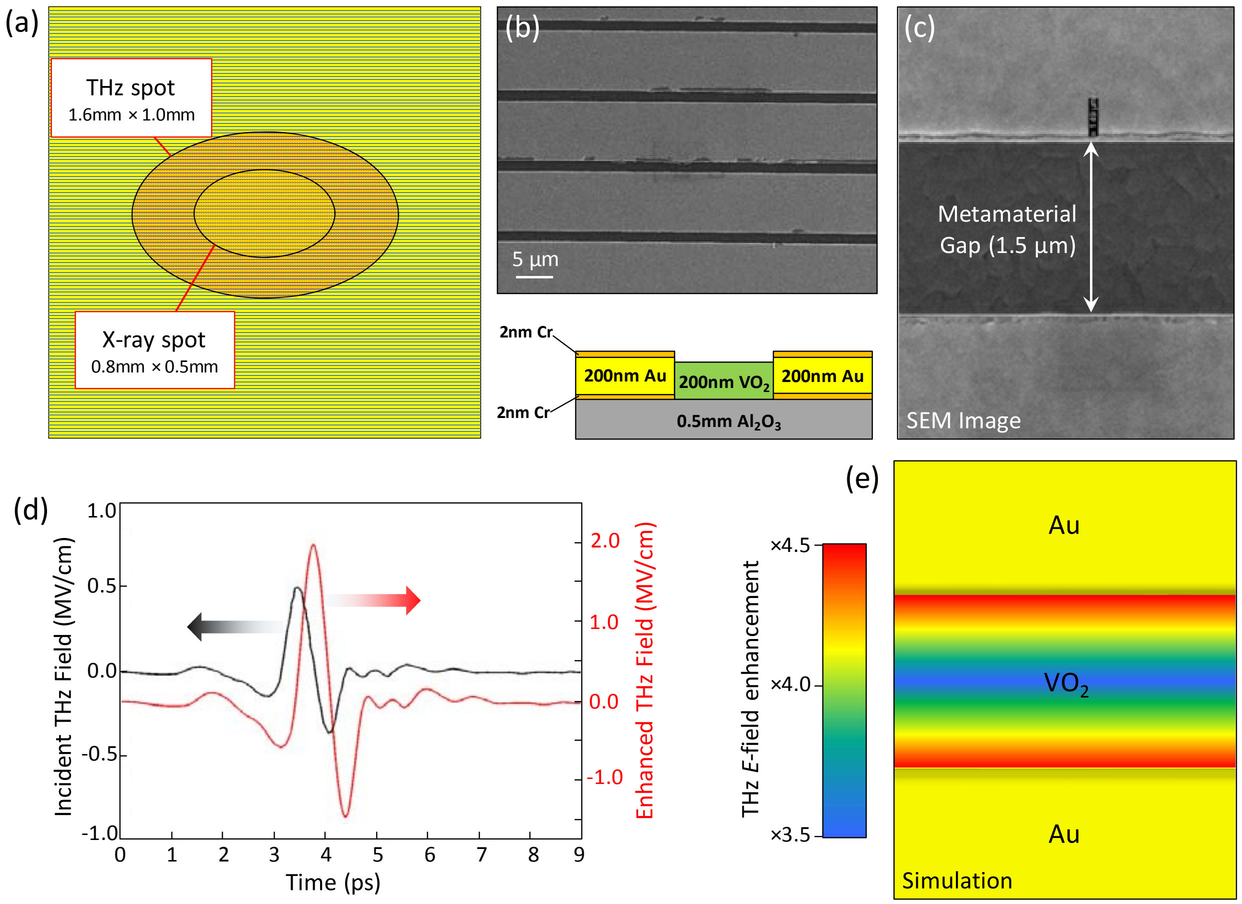

FIG. 2. THz metamaterials simulations and characterization. (a) Schematic diagram depicting relative scales of the metamaterials grid pattern, THz beam footprint on the sample (1.6 mm × 1.0 mm) and the x-ray beam footprint on the sample (0.8 mm × 0.5 mm). (b) Scanning electron microscopy (SEM) image of the optimized periodic metamaterials pattern showing wider Au lines (8.5 µm) and narrower (1.5 µm) gaps exposing the VO_2 film (dark contrast). Cross sectional profile of the structure is shown below. 2 nm-thick Cr layers are used to optimize the adhesion and lift-off steps during the lithography process. (c) High-resolution SEM image of the 1.5 µm-wide metamaterial gap exposing the VO_2 film. (d) Simulated time-dependent THz field (red) in the metamaterial gaps using experimental data (black) as the input. (e) THz field enhancement as a function of position within the 1.5 µm gap, showing an average field enhancement of ×4. The chosen geometry represents a compromise between substantial field enhancement for the THz pump and fill fraction of VO_2 for adequate sampling using the x-ray probe. The chosen design further minimizes non-uniformity of the electric field inside of the gap.

FIG. 3

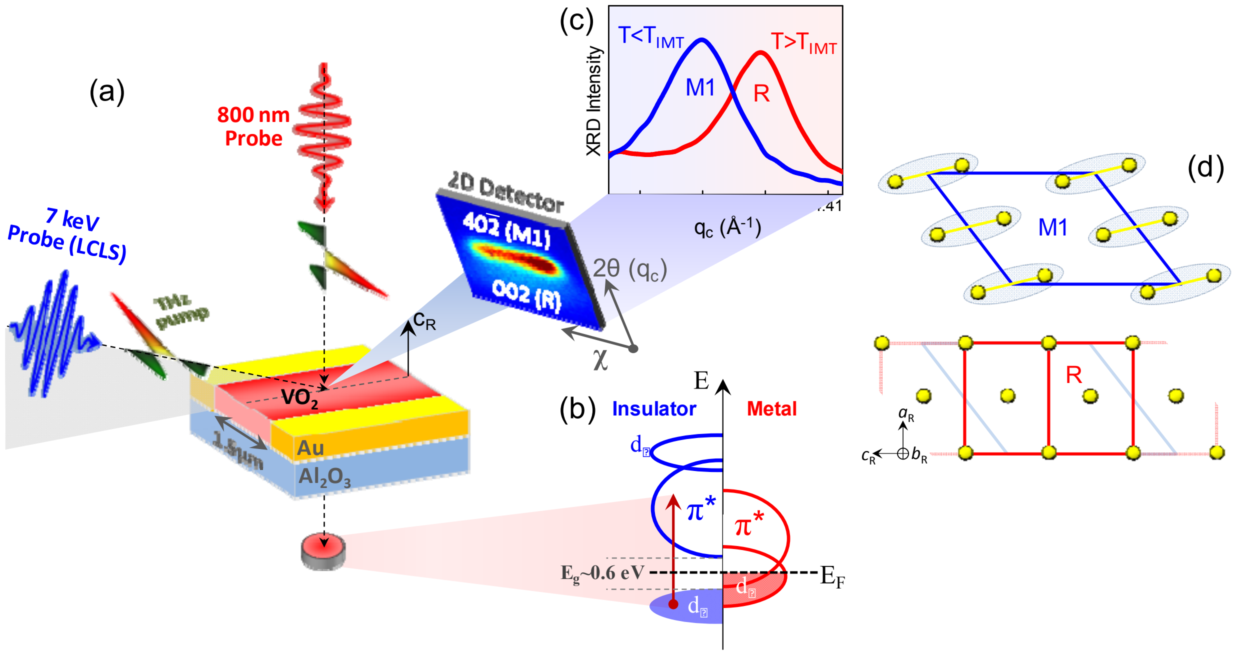

FIG. 3. Schematic of the THz-pump x-ray probe experiment at LCLS and the relevant observable processes. (a) The single-cycle THz pump pulse and the 7 keV hard x-ray probe pulse are incident on the sample in collinear Bragg-diffraction geometry, while the THz-pump 800-nm probe measurements are carried out in a normal-incidence transmission geometry. The electric field of the THz pulse is locally enhanced at the sample surface using linear arrays of plasmonic metamaterial antennae. (b) Schematic diagram of the equilibrium VO_2 band structure near the Fermi level in its insulating and metallic states. (c) Static θ-2θ spectroscopic calibration measurements of the monoclinic ($40\bar{2}$) and rutile (002) diffraction peaks (marked M1 and R, respectively) at temperatures well below and above T_{IMT} using the 2D detector. (d) In the low-temperature ($T<T_{IMT}$) phase VO_2 has a $P2_1/c$ monoclinic crystal structure characterized by dimerization of the neighboring V atoms along the c_R direction. In the high-temperature ($T>T_{IMT}$) phase the lattice undergoes a structural transition to a higher-symmetry $P4_2/mnm$ rutile structure, clearly discernable via hard x-ray scattering (see (a) and (c)).

FIG. 4

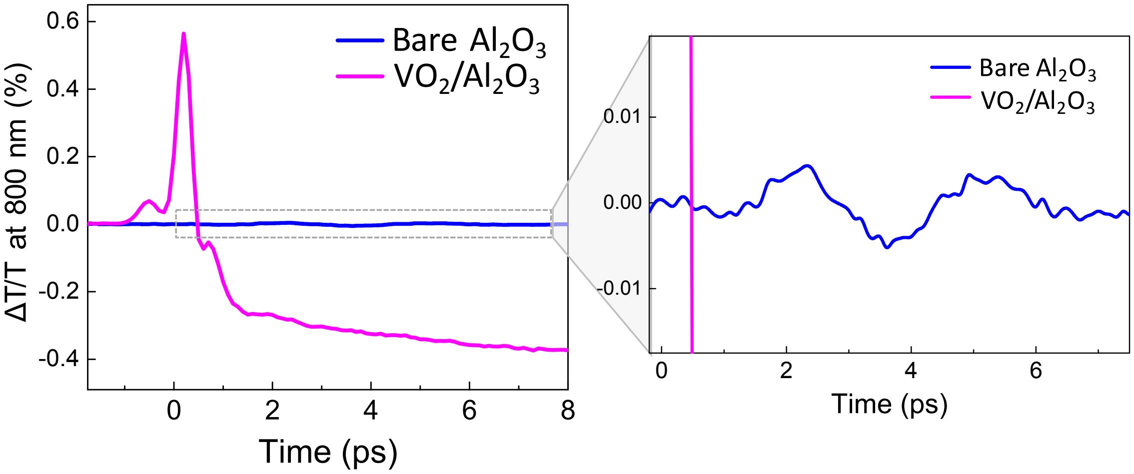

FIG. 4. Substrate response to the THz *E*-field pump. THz-pump - near-IR-probe change in transmission response for the bare Al_2O_3 substrate (blue) compared to that of a 200 nm VO_2 film on the same Al_2O_3 substrate (magenta). The Al_2O_3 substrate shows almost no measurable response to the THz pulse, except for small-amplitude ps-scale modulations between 2 and 6 ps (outset) which are orders of magnitude weaker than the VO_2 response.

FIG. 5

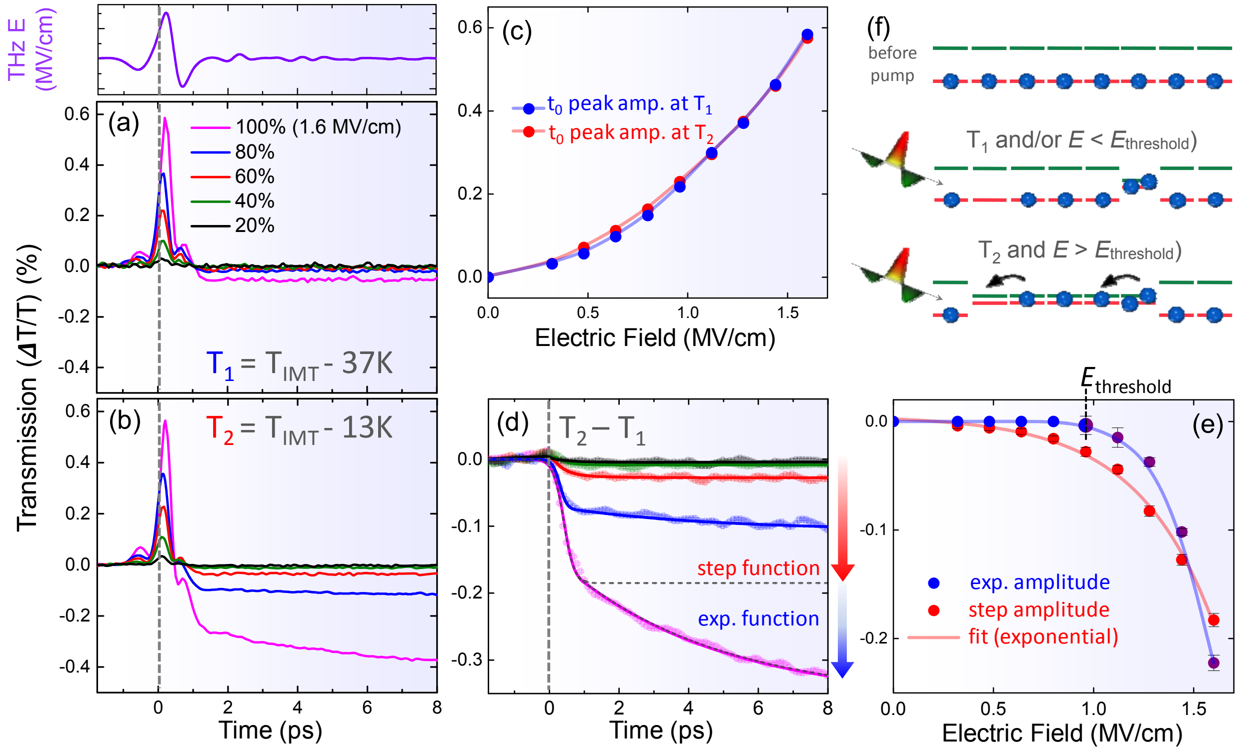

FIG. 5. Electronic dynamics in a VO$_2$ thin film undergoing an IMT induced by an ultrafast THz electric-field pulse (shown in the outset). (a) The *E*-field dependent electronic response measured via near-IR transmission at room temperature (T$_1$=300 K) is dominated by a sharp transient increase in transmission consistent with Wannier-Stark-like band renormalization [3,33-38]. For high fluences (*e.g.* purple delay trace) this process is accompanied by a weak concomitant drop in transmission, characteristic of sudden metallization of VO$_2$ via direct Zener-Keldysh-like interband tunneling [38-42]. (b) At the onset of the IMT (T$_2$=T$_{IMT}$-13 K) tunneling processes become more efficient, and above a threshold peak-field of approximately 1 MV/cm the absorbed energy density is sufficient to initiate lattice dynamics (see Fig. 7). (c) Wannier-Stark peak amplitude exhibits a non-linear dependence on the peak *E*-field with minimal temperature dependence between 300 K and 324 K. (d) The subsequent dynamics can be pictured more clearly by subtracting off the temperature independent dynamics. In this plot, data shown in panel (a) is subtracted from the corresponding data from panel (b). (e) *E*-field dependence of the amplitudes characterizing the pulse-width-broadened step and exponential functions suggests different electronic origins of the two processes and reveals the threshold onset of the exponential feature. (f) Schematic representation of the early-time electronic dynamics. The scenarios discussed in the text are visualized by depicting schematic energy levels (metallic vs. insulating) for an atomic chain.

FIG. 6

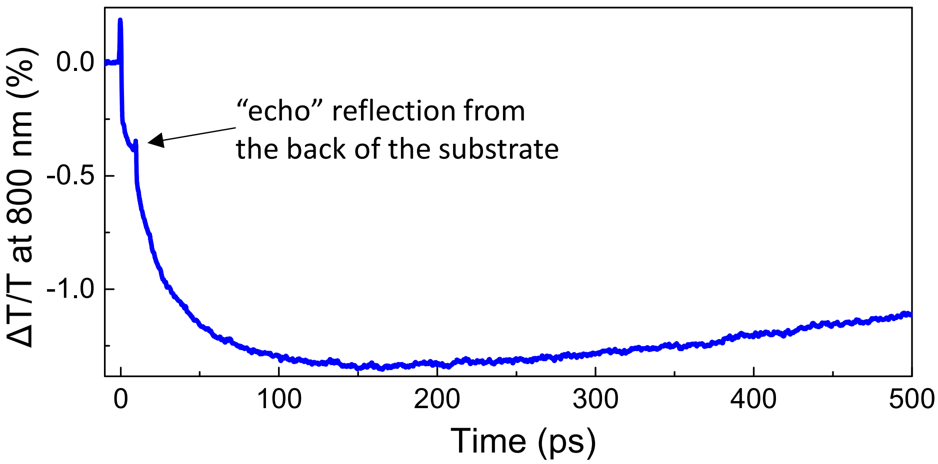

FIG. 6. THz-pump - near-IR-probe change in transmission for VO_2/Al_2O_3 for longer time delays. Transmission at 800 nm decays monotonically, with the exception of a sharp feature observed at *ca.* +9.5 ps time delay, which is an “echo” artefact, arising due to the reflection of the THz pulse from the backside of the substrate in the normal-incidence geometry.

FIG. 7

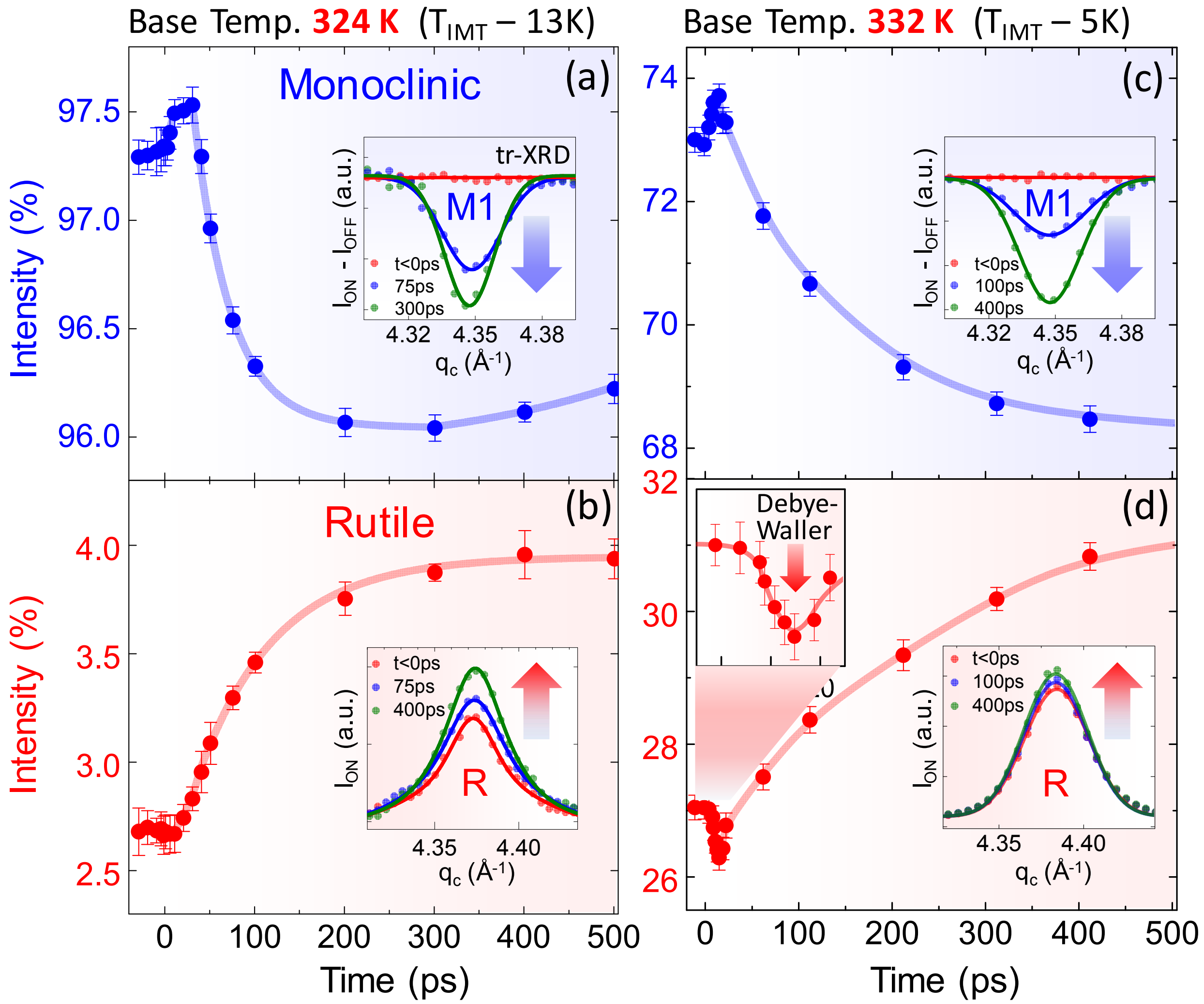

FIG. 7. Structural dynamics of the crystalline VO_2 (001) thin film undergoing an IMT induced by an ultrafast THz electric-field pulse with 1 MV/cm peak electric field. (a) and (b) Long-term temporal evolution of the monoclinic (a) and rutile (b) peak intensities, obtained via θ-2θ scans (shown in the insets) at each time delay at a base temperature of 324 K. (c) and (d) Temporal evolution of the monoclinic (c) and rutile (d) peak intensities at a higher base temperature of 332 K. The insets in panels (a)-(d) show the θ-2θ scans at key time delays - before the excitation (red), approximately half-way to the saturation point (blue), and near the saturation point (green). Experimental spectra (circular markers in the insets) were fitted using simple gaussians (solid lines) to obtain peak intensities as functions of time delays. For the monoclinic peak, since the intensity changes are significantly smaller compared to the absolute intensities of the peak in the

ground state (~73-97%), we show the angle-resolved intensity change spectra (I_{ON}-I_{OFF}). These were obtained by subtracting the reference θ-2θ scans recorded without the excitation laser pulse (I_{OFF}) from the normal scans obtained with the laser pulse (I_{ON}). Upper inset in panel (d) shows the initial suppression of the rutile x-ray diffraction signal (absent in (b)) for the first 15 ps due to preferential heating of the lattice in these metallic regions.